First example of protonation of Ruddlesden-Popper Sr_2IrO_4: a route to better water oxidation catalysts

*Ronghuang Zhang, Paul E. Pearce, Vanessa Pimenta, Mathieu Courty, Jordy Cabana, Heifang Li, Daniel Alves Dalla Corte, Artem M. Abakumov, Gwenaelle Rousse, Domitille Giaume, Michael Deschamps, Alexis Grimaud**

E-mail: alexis.grimaud@college-de-france.fr

Dr R. Zhang, Dr P. E. Pearce, Dr. D. A. D. Corte, Prof. G. Rousse, Dr A. Grimaud

Chimie du Solide et de l'Energie, UMR 8260, Collège de France, 75231, Paris Cedex 05, France

Réseau sur le Stockage Electrochimique de l'Energie (RS2E), CNRS FR 3459,33 rue Saint Leu, 80039, Amiens Cedex, France

Dr P. E. Pearce

Sorbonne Université, Paris, France

Prof V. Pimenta

Institut des Matériaux Poreux de Paris, UMR 8004 CNRS, Ecole Normale Supérieure, Ecole Supérieure de Chimie et de Physique Industrielle de Paris, PSL University, 75005, Paris, France Prof. A. Abakumov

Prof. J. Cabana, Dr H. Li
Advanced Photon Source, Argonne National Laboratory, Argonne, Illinois 60439, United States
#Department of Chemistry, University of Illinois at Chicago, Chicago, Illinois 60607, United States
@Joint Center for Energy Storage Research (JCESR), Argonne National Laboratory, Lemont, Illinois 60439, United States

Pro. A. M. Abakumov

Skoltech Center for Electrochemical Energy Storage, Skolkovo Institute of Science and Technology, Moscow 143026, Russia

Prof. D. Giaume

Chimie ParisTech, PSL University, CNRS, Institut de Recherche de Chimie Paris, 75005 Paris, France

Prof M. Deschamps

CNRS, CEMHTI UPR3079, Université d'Orléans, 1D avenue de la recherche scientifique, 45071 Orléans Cedex 2, France

ALISTORE-European Research Institute, FR CNRS 3104, 80039 Amiens, France

Keywords: water oxidation, oxygen evolution reaction, iridium oxide, protonated phase, cation exchange

Abstract: Water electrolysis is considered a promising way to store and convert excess renewable energies into hydrogen, which is of high value for many chemical transformation processes such as the Haber-Bosch process. However, to take advantage of the polymer electrolyte membrane (PEM) technology, the main challenge lies in the design of robust catalysts for oxygen evolution reaction (OER) under acidic conditions since most of transition metal based complex oxides used undergo structural degradation under these harsh acidic conditions. To broaden the variety of candidate materials as OER catalysts, a cation-exchange synthetic route was recently explored to reach crystalline pronated iridates with unique structure and properties. In this work, a new protonated phase $H_{3.6}IrO_4 \cdot 3.7H_2O$, prepared via Sr^{2+}/H^+ cation exchange at room temperature starting from the parent Ruddlesden-Popper Sr_2IrO_4 phase, is described. This is the first discovery of crystalline protonated iridate forming from a perovskite-like phase, and adopting a layered structure with apex-linked IrO_6. Furthermore, $H_{3.6}IrO_4 \cdot 3.7H_2O$ is found to possess not only an enhanced specific catalytic activity, superior to that of other perovskite-based iridates, but also a mass activity even comparable to that of nanometric IrO_x particles, while showing an improved catalytic stability owing to its ability to reversibly exchange protons in acid.

1. Introduction

Clean production of hydrogen via water electrolysis has long been envisioned as a key process to store and convert renewable energies. Indeed, hydrogen is critical for many applications, such as the transformation of nitrogen into ammonia through the Haber-Bosch process which contributes more than 1% of the annual energy consumption. Currently, the production of hydrogen still largely relies on fossil fuel reforming, a process which emits CO_2. Water electrolysis ($H_2O = H_2 + O_2$), though considered as an appealing way to achieve clean hydrogen production, only represents around 4% of the annual total, mostly as a side product of the chloralkali process, due to associated technological difficulties.

At present, alkaline water electrolyzers (AWE) are used to realize water electrolysis at industrial scale. However, their performance remains limited owing to the large ohmic drop encountered in the cell that uses alkaline solutions in combination with a diaphragm. Instead, polymer electrolyte membrane water electrolyzers (PEMWE) use a proton conducting membrane, which has the advantage of avoiding the use of large quantity of electrolyte and hence decreasing the ohmic drop in the cell.[1][2] Nevertheless, despite the clear advantages of this technology, the use of acidic conditions as imposed by the protonic conducting membrane leads to drastic instabilities of the catalysts. This is especially true with respect to catalysts for the oxygen evolution reaction (OER), one of the half reactions during water electrolysis that oxidizes water to produce oxygen. Currently, only iridium-based catalysts are considered as sufficiently stable in the harsh acidic conditions required by the PEMWE technology. However, the main issue regarding the use of iridium-based oxides as OER catalysts arises from the scarcity of iridium, whose annual production is even lower than that of platinum by as much as two orders of magnitude.[3] New chemical strategies to develop better iridium-based OER catalysts both in terms of specific activity (i.e. activity normalized by surface active sites) as well as mass activity are therefore of prime importance for the development of PEMWE.[4][5][6]

Towards this goal of improving the performances of Ir-based OER catalysts, several strategies were recently proposed. Among them, the use of amorphous and hydrated IrO_x as well as iridium-based perovskites as OER catalysts appear promising.[7][8][9][10][11][12][13][14] Nevertheless, despite the high catalytic activity of these OER catalysts, their stability is limited compared to the conventional IrO_2.[15] Specific research efforts are therefore dedicated to limit the dissolution of iridium under OER conditions.[16] Recently, we demonstrated that cationic exchange can be used to prepare a series of novel protonated iridates with improved catalytic stability,[17][18] owing to their ability to reversibly exchange protons under acidic conditions and, therefore, to compensate a charge modification associated with the oxidation of iridium resulting from cation leaching as well as its chemical reactivity with water. This charge

compensation via proton exchange helps to avoid the formation of soluble Ir^{3+} or IrO_4^{2-} species in what is considered as the dominating mechanism of iridium dissolution.[19] However, the cation exchange strategy was so-far limited to monovalent Li^+/H^+ exchange starting from a parent Li_xIrO_y phase.[20] Cation exchange between divalent cations and protons, such as AEM^{2+}/H^+ exchange (AEM: alkaline earth metal), has not been reported for perovskites so far. Instead, structural degradation of these complex oxides was often observed upon cation leaching under acidic conditions, leading to their poor overall catalytic stability.[21][14][22] This lack of cation exchange is likely due to the great size and charge differences in between AEM^{2+} and H^+, which would introduce significant lattice strains on the 3D-linked IrO_6-network of the perovskite and thus compromises its structural integrity. Therefore, for perovskite-like materials reported up to date such as $SrIrO_3$, Sr_2IrCoO_6 or Ba_2LnIrO_6, no crystalline protonated iridate was obtained via cationic exchange, while the formation of amorphous iridium oxide, usually denoted as $IrO_x{\cdot}nH_2O$, was instead commonly observed on their surfaces.[11][14][22] All in all, the structural instability of most of complex oxides, including perovskites, when interacting with H^+ imposes great limits on our ability to design better OER catalysts for PEMWE.

In this work, we report the discovery of a new protonated phase $H_{3.6}IrO_4{\cdot}3.7H_2O$ prepared via Sr^{2+}/H^+ cation exchange at room temperature starting from the parent Ruddlesden-Popper Sr_2IrO_4 phase. This new protonated iridate adopts a layered structure with apex-linked IrO_6 and is, to the best of our knowledge, the first example of crystalline protonated iridate forming from a perovskite-like phase. Furthermore, we demonstrate that $H_{3.6}IrO_4{\cdot}3.7H_2O$ not only exhibits an enhanced OER activity superior to other perovskite-based iridates and even comparable to the performances obtained for nanometrics IrO_x particles, but also improved catalytic stability under OER conditions owing to its ability to reversibly exchange protons in acidic conditions.

2. Results

2.1. Synthesis, composition and structure of the newly formed protonated phase

The novel protonated iridate H_xIrO_y was obtained via a cation exchange of H^+/Sr^{2+} starting from the Sr_2IrO_4 Ruddlesden-Popper (RP) phase, as illustrated in Figure 1. In brief, Sr_2IrO_4 powder was stirred in 0.1 M $HClO_4$ for 12 h, then recovered by centrifugation and dried at 55 °C under vacuum. The formation of a novel phase was confirmed by X-ray diffraction (XRD, Figure 1b) collected on the powder recovered after drying, where peaks that cannot be indexed into the space group of the parent Sr_2IrO_4 phase were observed. Complete dissolution of Sr^{2+} from Sr_2IrO_4 was confirmed by energy-dispersive X-ray (EDX) analysis (see Supplementary Information (SI), Figure S1). The composition of the newly obtained H_xIrO_y phase was then characterized by thermogravimetric analysis coupled with mass spectrometry (TGA-MS) (Figure 2a, detailed in the Experimental Section). According to the TGA-MS results, H_xIrO_y first loses structural water to form rutile-IrO_x in the temperature range 140 - 400 °C, before decomposing into metallic Ir when heating up to 1000 °C under Ar. The formation of rutile-IrO_x at 400 °C and Ir at 1000 °C was confirmed by the X-ray diffraction data collected at the corresponding temperatures, as shown in Figure S2 in the SI. From the weight loss measured by TGA, the H_2O content in H_xIrO_y is estimated to be 5.50(5). Coupling this result to the amount of oxygen loss during the decomposition into Ir, the composition of the newly obtained hydrated iridate is thus determined to be $H_{3.6}IrO_4 \cdot 3.7H_2O$, given that Sr^{2+} is fully replaced by H^+ during the cation exchange as suggested by EDX analysis (Figure S1). Furthermore, despite the striking size and charge differences existing between H^+ and Sr^{2+}, the cation exchange process merely jeopardized the morphology of the particles where particles largely retained their shape and size during the cation exchange, as observed by SEM (inset of Figure 1a and 1b). Nevertheless, cracks can be observed on the particles after the cation exchanged step, possibly

due to a moderate exfoliation process occurring during the insertion of H^+/H_2O into the layered iridate and the subsequent drying step.

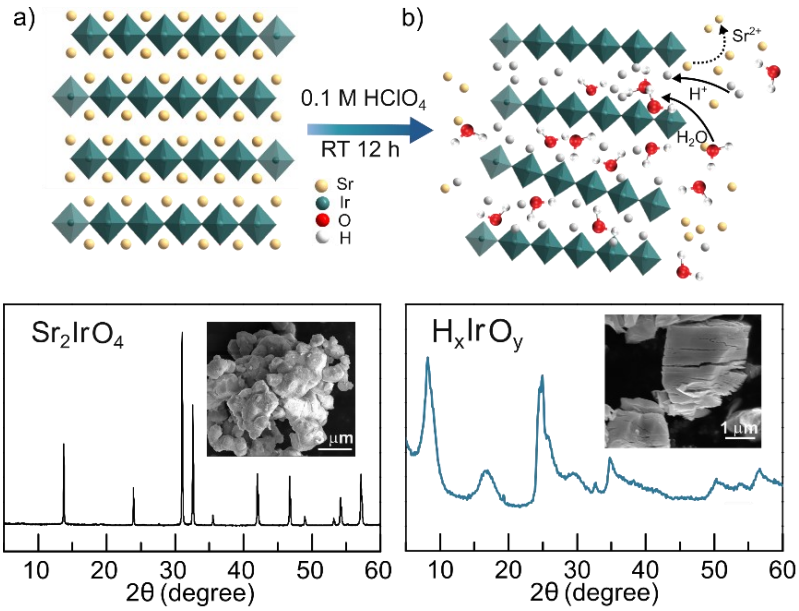

Figure 1. a Crystallographic structure of the parent Sr_2IrO_4 phase and **b** schematic representation of the hydrated $H_{3.6}IrO_4 \cdot 3.7H_2O$ phase obtained after cation exchange as well as their corresponding powder XRD patterns (bottom) and SEM images (insets).

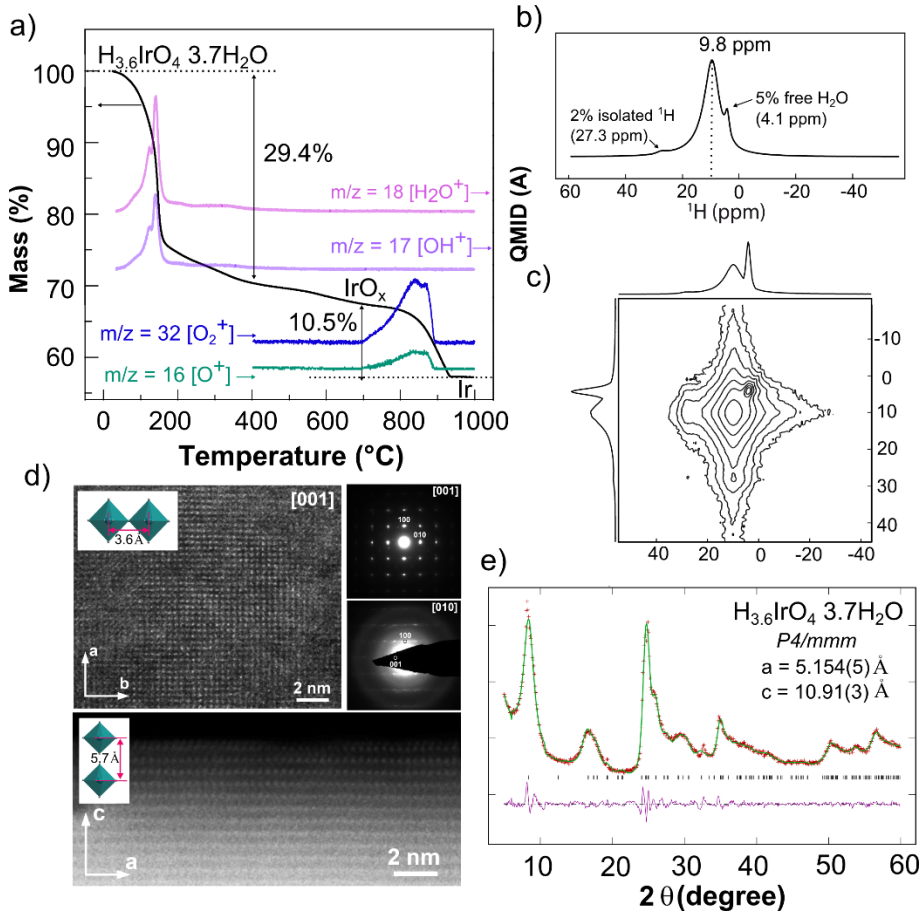

Figure 2. a Thermogravimetric analysis with mass spectrometry (TGA-MS) curve, **b** ^{1}H solid-state nuclear magnetic resonance (NMR) spectra, **c** ^{1}H 2D exchange NMR spectra, **d** HRTEM images as well as ED patterns in the [001] and [010] orientation and **e** Le Bail fit of the powder XRD data collected from the $H_{3.6}IrO_4 \cdot 3.7H_2O$ hydrated phase.

To investigate the proton environment in $H_{3.6}IrO_4 \cdot 3.7H_2O$, solid-state ^{1}H nuclear magnetic resonance (NMR) measurements were carried out at room temperature (Figure 2b and 2c). One major broad ^{1}H peak centered at 9.8 ppm is observed and can be assigned to structural protons in $H_{3.6}IrO_4 \cdot 3.7H_2O$ (Figure 2b). Given that no obvious splitting was observed for this peak at 9.8 ppm, it is reasonable to conclude that, in $H_{3.6}IrO_4 \cdot 3.7H_2O$, the protons bound to IrO_6 octahedra have similar average environment and that they are in fast exchange with structural water molecules which usually shows a lower chemical shift, thus giving rise to a broad ^{1}H signal. Apart from this main peak, a sharp shoulder peak is observed at 4.1 ppm and can be

assigned to H_2O [ref], suggesting the presence of a small portion of "free" water (5%), i.e. water molecules not interacting with structural protons, for the newly formed iridate. Furthermore, a very small fraction of isolated protons (2%) was also observed at 27.3 ppm. As these two minority proton peaks do not exchange with the main peak at 9.8 ppm, as observed in the two-dimensional exchange spectrum (Figure 2c), one can conclude that these peaks represent water molecules and protons on the surface of the particles rather than in the bulk.

As observed in the XRD pattern in Figure 1b, the newly obtained $H_{3.6}IrO_4 \cdot 3.7H_2O$ is poorly crystallized, challenging its structural characterization solely by powder XRD. Thus, to gain insight into the structure of this protonated iridate, electron diffraction (ED) and high angle annular dark field scanning transmission electron microscopy (HAADF-STEM) images were taken (Figure 2d). The ED data of $H_{3.6}IrO_4 \cdot 3.7H_2O$ could be indexed into a primitive tetragonal unit cell with $a \approx 3.6$ Å, $c \approx 5.7$ Å, or a cell with $\sqrt{2} \times \sqrt{2} \times 2$ expansion ($a \approx 5.1$ Å, $c \approx 11.4$ Å). Furthermore, the HAADF-STEM image in the [001] direction reveals that the $H_{3.6}IrO_4 \cdot 3.7H_2O$ phase consists of layers of iridium with an Ir-Ir distance of 3.6 Å, characteristic of apex linked IrO_6 octahedra (~ 3.8 and ~ 3.0 Å in general for corner- and edge-shared IrO_6, respectively). Moreover, the image in the [010] direction shows that these corner-shared iridium layers are separated by ~ 5.7 Å with oxygen atoms facing each other. Based on these results, a LeBail refinement against the X-ray diffraction data of $H_{3.6}IrO_4 \cdot 3.7H_2O$ using a tetragonal *P4/mmm* model with $a \approx 5.154(4)$ Å, $c \approx 10.91(3)$ Å was conducted (Figure 1e), and the refined structure is shown in Figure 3a. From the refined structure, one can observe that the H^+/Sr^{2+} cation exchange led to a structural modification of the parent RP phase, Sr_2IrO_4 (Figure 1a). While the apex linked IrO_6 octahedra in each iridium layer in the *ab* plane is retained, the cation exchange triggers a gliding of the iridium layer along the [110] direction alternatively so that every IrO_6 octahedra sits on top of each other. This gliding is possibly driven by protonation of apical oxygen that screens the repulsion between each oxygen layers combined with the

intercalation of a large amount of structural water molecules into interstitial sites with a dimension of ~2.5 × 2.2 × 3.6 $Å^3$ in the new structure, as depicted in Figure 3b. Moreover, as suggested by the ^1H NMR results (Figure 2b), the apical oxygens are presumably protonated with almost two protons so that all the protons sit in a similar environment and are in direct exchange with structural water molecules that sit in the interstitials.

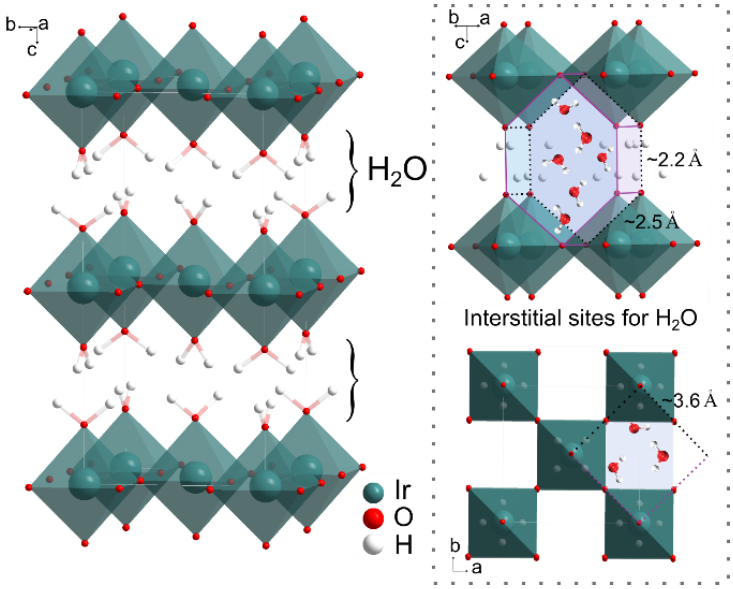

Figure 3. Schematic representation of the structure of the new hydrated $H_{3.6}IrO_4 \cdot 3.7H_2O$ phase. The corner-shared octahedral as well as the protons positions are extrapolated for the structural model deduced from the XRD, HRTEM and NMR results (left), while the structural water molecules which are interacting with protons on apical oxygen are schematically represented in the interstitial positions created in the new structure (right).

Altogether, these results indicate that $H_{3.6}IrO_4 \cdot 3.7H_2O$ is, to the best of our knowledge, the first pronated iridate with a perovskite-like structure reported to date. Other iridium-based perovskites such as $SrIrO_3$ or Sr_2IrFeO_6 have been observed to either collapse or to heavily dissolve before precipitating into amorphous hydrated IrO_x when placed in acidic conditions.[11][14][22] The successful H^+/Sr^{2+} exchange to form $H_{3.6}IrO_4 \cdot 3.7H_2O$ starting from the parent phase Sr_2IrO_4 certainly benefits from the structural flexibility offered by the layered

nature of the parent RP phase in which cations can tunnel in/out without deconstructing the in plane corner-shared coordination of the IrO_6 octahedra. Furthermore, RP phases are known to accommodate interstitial anions such as O^{2-} within their structure[23][24], thus allowing the co-intercalation of structural water molecules during the cation exchange which, by hydrogen bonding, stabilizes the structural protons. Unlike the 2D RP phase, the H^+/Sr^{2+} exchange in cubic or hexagonal perovskite such as $SrIrO_3$ would introduce significant lattice strains on its 3D IrO_6-network and thus compromise the structural integrity of the parent phase, leading to a dissolution of the phase and a precipitation of amorphous IrO_x compounds on its surface. New families of novel protonated iridates, such as the H_xIrO_3 and H_xIrO_4 series, have been recently reported.[17][20] However, $H_{3.6}IrO_4{\cdot}3.7H_2O$ differs distinctively from these oxides, which were previously synthetized via a Li^+/H^+ exchange step in acid from the parent β-Li_2IrO_3 and Li_3IrO_4 phases, respectively. Unlike the H_xIrO_3 and H_xIrO_4 series whose structures consist of edge-sharing IrO_6 octahedra conserved from their parent phases during cation exchange, the newly obtained $H_{3.6}IrO_4{\cdot}3.7H_2O$ contains layers of corner-sharing IrO_6 octahedra, with a large amount of structural water accommodated following a non-topotactic reaction. The layered perovskite-like structure adopted by $H_{3.6}IrO_4{\cdot}3.7H_2O$ is also uniquely distinct from previously reported IrOOH via ion exchange from its structural relative $K_{0.75}Na_{0.25}IrO_2$,[25] which consists of trigonal layers of edge-sharing octahedra.

2.2. Electrocatalytic properties towards OER

Having determined the crystal structure for the newly obtained $H_{3.6}IrO_4{\cdot}3.7H_2O$ phase, its electrochemical performance towards water oxidation was tested in 0.1 M $HClO_4$ and compared with Sr_2IrO_4 (Figure 4a and Figure S3). No major difference in their respective redox activity was observed between the two phases. This observation indicates that the parent Sr_2IrO_4 phase quickly transforms into the protonated phase after exposure to the acidic environment, reinforcing that the cation Sr^{2+}/H^+ exchange is fast in acidic conditions. Nevertheless, while

their redox behaviors were found similar, such a phase transformation induces a significant change in the specific surface area of the iridate, as revealed by Brunauer-Emmer-Teller (BET) method. The BET surface area of the pristine Sr_2IrO_4 was measured to be 0.30 m^2/g, a limited specific surface area commonly observed for crystalline oxide catalysts synthesized by solid-state reaction at high temperature, while the surface area of the exchanged phase $H_{3.6}IrO_4 \cdot 3.7H_2O$ was measured to be 4.01 m^2/g, ~13 fold larger than that of the pristine Sr_2IrO_4 before exchange. This drastic gain in surface area presumably results from the cracks observed by SEM, as discussed in Figure 1b. Therefore, caution must be exercised when normalizing the OER performances of a catalyst using the BET surface area of the pristine compound, especially when the catalyst undergoes phase transformation upon interaction with the electrolyte (e.g. ion exchange, dissolution, element leaching). For instance, if the OER performances for Sr_2IrO_4 were normalized by the BET surface area of the pristine phase (~ 0.3 m^2/g), a current as high as 10 mA/cm^2_{oxide} would be obtained at 250 mV overpotential (red dashed line in Figure 4b), outperforming most of iridium-based oxides reported to date. However, the "real" performances for the $H_{3.6}IrO_4 \cdot 3.7H_2O$ phase are found one order of magnitude lower, but still among the most active iridate oxides previously reported (red line in Figure 4b).

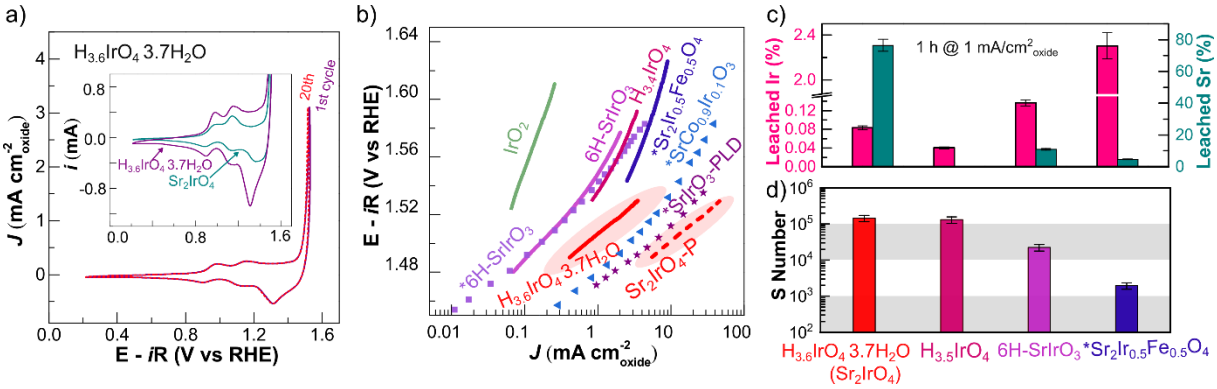

Figure 4. a Representative CV scans obtained directly from the cation-exchanged phase $H_{3.6}IrO_4 \cdot 3.7H_2O$ compared to those obtained from the parent phase Sr_2IrO_4 with no exchange prior to OER measurements. **b** Tafel slopes for the OER activity normalized by BET surface area for selected iridium-based catalysts compared to the one obtained for $H_{3.6}IrO_4 \cdot 3.7H_2O$

when normalized with the BET surface measured before (red solid line) or after (red dash line) cation exchange. **c** Amount of iridium and strontium detected by ICP measurements after electrochemical testing for 1h at 1 mA/cm²oxide (top, error bar: 10 %). **d** Calculated stability number (S-number) for $H_{3.6}IrO_4 \cdot 3.7H_2O$ compared to selected iridium-based catalysts (bottom, error bar 20 %).

As shown in Figure 4b, a current density of 4.0 mA/cm^2_{oxide} is obtained for $H_{3.6}IrO_4 \cdot 3.7H_2O$ at an overpotential of 300 mV, ~2 fold that of Ir^V-based $Sr_2Ir_{0.5}Fe_{0.5}O_4$ (2.0 mA/cm^2_{oxide}, BET = 0.75 m^2/g), ~5 fold that of $H_{3.5}IrO_4$ (0.75 mA/cm^2_{oxide}, BET = 2.2 m^2/g) and ~7 fold that of 6H-$SrIrO_3$ (0.56 mA/cm^2_{oxide}, BET = 1.0 m^2/g). Only the OER performance obtained for $SrIr_{0.1}Co_{0.9}O_3$ (~9 mA/cm^2_{oxide}, BET = 0.175 m^2/g) and for epitaxial $SrIrO_3$ film (~20 mA/cm^2) were found to be greater. Nevertheless, doubts arise from the proper normalization of such catalysts undergoing phase transformation and surface reconstruction into IrO_x in acid, as pointed out in a recent work.[26] Interestingly, the newly obtained $H_{3.6}IrO_4 \cdot 3.7H_2O$ phase exhibits greater OER performances when compared to another layered iridate, namely $H_{3.5}IrO_4$[20]. The superior activity of $H_{3.6}IrO_4 \cdot 3.7H_2O$ can be tentatively explained by the corner-sharing IrO_6 network within its structure, with earlier reports proposing that catalysts containing corner-shared BO_6 are preferred for the OER.[27] Furthermore, the presence of large amount of structural water in $H_{3.6}IrO_4 \cdot 3.7H_2O$ might influence the formation energy of the OER intermediates (*OH, *O, and *OOH), as proposed in earlier reports where hydroxylated RP-perovskite $Sr_3FeCoO_{7-\delta}$ was found to have enhanced OER activity.[28]

Having established that the OER performances measured for $H_{3.6}IrO_4 \cdot 3.7H_2O$ are among the best for iridium-based oxide catalysts so far reported, we then investigated the stability of this catalyst in OER conditions. The amount of dissolved iridium was tracked down by inductively coupled plasma atomic emission spectroscopy (ICP-OES) under galvanostatic conditions at 1.0 mA/cm^2_{oxide} for 1 h (see details in the Experimental Section). As shown in

Figure 4c, the percentage of leached iridium for several iridium-based oxides trends was as follows: $H_{3.5}IrO_4$ < $H_{3.6}IrO_4 \cdot 3.7H_2O$ < 6H-$SrIrO_3$ << $Sr_2Ir_{0.5}Fe_{0.5}O_4$, suggesting that $H_{3.5}IrO_4$ and $H_{3.6}IrO_4 \cdot 3.7H_2O$ are relatively more stable (see Table S1 for the raw current and measured potentials for each catalyst). Moreover, the relative stability of this protonated phase is reinforced by the evaluation of the 'stability number' (S-number), previously defined as the ratio of gaseous oxygen generated during OER and the amount of dissolved iridium.[22] For $H_{3.6}IrO_4 \cdot 3.7H_2O$, the S-number is calculated to be ~10^5, approximating the one obtained for $H_{3.5}IrO_4$ (~10^5) and greater than for 6H-$SrIrO_3$ (~10^4) and $Sr_2Ir_{0.5}Fe_{0.5}O_4$ (~10^3). As a comparison, rutile-IrO_2 and IrO_x have been reported to have an S-number of ~10^6 and ~10^5, respectively.[22] Thus, the S-numbers for protonated iridates $H_{3.6}IrO_4 \cdot 3.7H_2O$ and $H_{3.5}IrO_4$ are similar to IrO_x and only below rutile-IrO_2, while the OER activity of $H_{3.6}IrO_4 \cdot 3.7H_2O$ outperforms both of these compounds. Furthermore, it is interesting to point out that $H_{3.6}IrO_4 \cdot 3.7H_2O$ prepared from the parent RP-Sr_2IrO_4 phase is significantly more stable than the Fe-doped RP-perovskite $Sr_2Ir_{0.5}Fe_{0.5}O_4$, as seen by the increase of ~2 orders of magnitude in S-number (Figure 4c). This difference can be easily explained by the fact that $Sr_2Ir_{0.5}Fe_{0.5}O_4$ tends to heavily dissolve into acid while Sr_2IrO_4 undergoes cation exchange to form the protonated iridate, $H_{3.6}IrO_4 \cdot 3.7H_2O$. These differences highlight that the substitution of Ir by a soluble element in acid (Fe) will only destabilize the layered iridate because leaching of Fe will break the bonding around IrO_6, causing the heavy dissolution of undercoordinated Ir in $Sr_2Ir_{0.5}Fe_{0.5}O_4$.

2.3. Proton exchange properties

To further understand the electrochemical behavior of $H_{3.6}IrO_4 \cdot 3.7H_2O$ and its ability to reversibly exchange protons in acidic conditions, its redox behavior was investigated in the potential range of 0.3 to 1.4 V vs RHE, prior to the OER potential. As shown in Figures 5a and 5b, two redox peaks are visible for $H_{3.6}IrO_4 \cdot 3.7H_2O$ in this potential range, with a first one

observed at ~0.92 V vs RHE, with a peak separation of ~50 mV, and a second one at ~1.14 V vs RHE, associated with a small peak separation of ~5 mV. These redox features are distinctively different to that reported for IrO_2,[22] IrO_x,[22][29] 6H-$SrIrO_3$[21] or $SrIrO_3$ epitaxial thin films[22], for instance. To gain further insight into the kinetics of these two redox peaks, cyclic voltammograms were collected as a function of the scan rate (Figure 5a and 5b). The intensity of the first redox peak at ~0.92 V vs RHE was found to be proportional to the square root of the scan rate, suggesting a bulk diffusion-limited redox process (Figure 5b). The intensity of the second redox peak at ~1.14 V vs RHE was found proportional to the scan rate (Figure 5a and b), suggesting a non-diffusion-limited surface proton exchange, agreeing with the small peak separation (~5 mV). These results are consistent with the ex-situ XRD data collected at different potentials for $H_{3.6}IrO_4 \cdot 3.7H_2O$ (see Experimental Section). It is worth mentioning that the patterns from electrodes were slightly different from a powder sample, possibly due to the preferred orientation of the layered $H_{3.6}IrO_4 \cdot 3.7H_2O$ and a slight loss of the structural water during the electrode preparation. Nevertheless, from these measurements one can observe that, as shown in Figure 5d, when scanning from the OCV to 1.3 V vs RHE, the (001) diffraction peak of $H_{3.6}IrO_4 \cdot 3.7H_2O$ at ~10° shifted to higher angle, indicating a decrease of *c* lattice parameters. This bulk contraction in the *c* direction can be ascribed to the removal of structural water and protons from $H_{3.6}IrO_4 \cdot 3.7H_2O$, a bulk process which is therefore diffusion-limited. From 1.3 V to ~1.5 V vs RHE where the OER occurs, no obvious change was observed in the XRD data, consistent with a surface process. When scanning back to the starting potential, a small shift of the (001) diffraction peak at ~10° as well as a change of the (003) and (110) diffraction peaks was observed, presumably due to the re-protonation of the $H_{3.6}IrO_4 \cdot 3.7H_2O$ in this potential range. Nevertheless, the XRD data collected back at the OCV for $H_{3.6}IrO_4 \cdot 3.7H_2O$ does not superimposed with that of the pristine phase, suggesting an irreversible loss of structural water upon cycling. Several reasons could explain this loss. First, reinsertion of structural water can be hindered by the presence of hydrophobic PTFE binder

used for preparing the electrode. Second, the diffusion-limited structural exchange of water might be kinetically hindered.

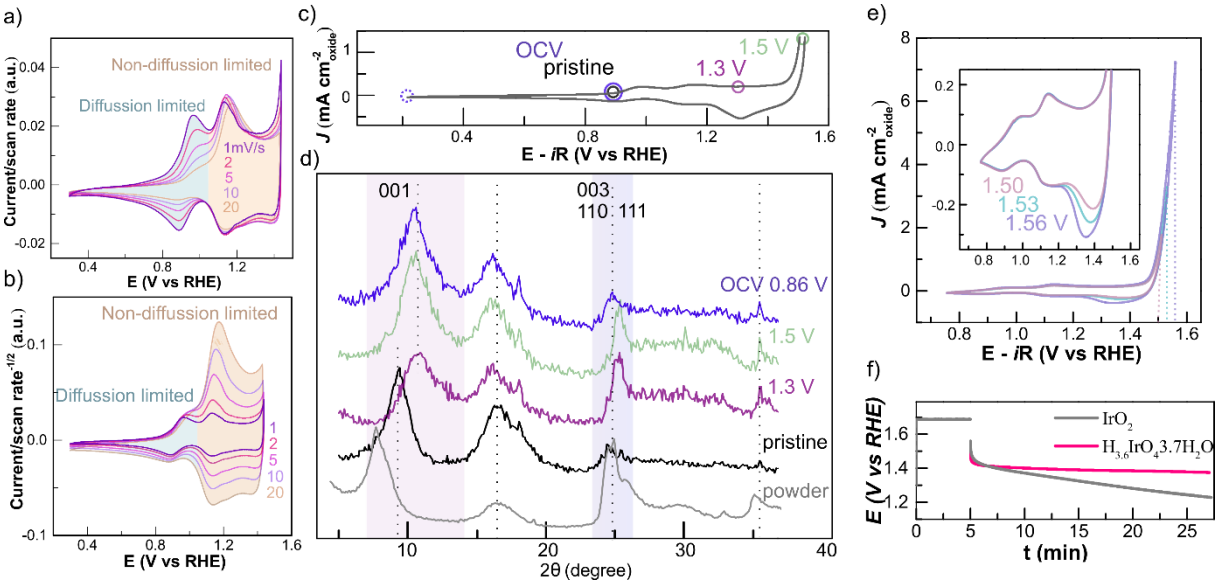

Figure 5. CV scans recorded at different scan rate for $H_{3.6}IrO_4 \cdot 3.7H_2O$ normalized by **a** the scan rate or **b** the square root of the scan rate. **c** typical CV scan recorded for an electrode from which **d** ex situ XRD patterns were collected at different potentials. **e** CV scans recorded for the same electrode but with different voltage cutoff (1.50, 1.53 and 1.56 V vs. RHE) and **f** evolution of the potential measured for $H_{3.6}IrO_4 \cdot 3.7H_2O$ compared to IrO_2 after potentiostatic holding at 1.65 V vs. RHE for 5 minutes.

Finally, in addition to these two redox features, a reduction peak at ~1.4 V vs. RHE is observed. Further investigation reveals that the intensity of this reduction peak is proportional to the cut-off potential during the OER (1.50, 1.53 V or 1.56 V vs. RHE, as shown in Figure 5e). This result implies that the intensity of the reduction peak is related to the amount of charge passed at potentials above 1.4 V vs. RHE. Therefore, this behavior suggests that the oxidation state of the iridate is modified during the OER. In order to confirm this hypothesis, tests were made during which $H_{3.6}IrO_4 \cdot 3.7H_2O$ was held at 1.65 vs RHE for 5 min before opening the circuit and monitoring the potential decay upon time. As shown in Figure 5f, the potential of

the hydrated iridate is found to rapidly stabilize at around 1.4 V vs RHE, unlike crystalline IrO_2, for which the potential is found to constantly decay for more than 20 minutes down below 1.2 V vs. RHE. This measurement further confirms that the active form of the iridate is an oxidized phase formed at the OER potential and that this oxidation state is maintained even in contact with a strongly acidic solution. In contrast, when holding IrO_2 at OER potential, no bulk oxidation is occurring and the potential slowly decays back to its potential of zero charge. Altogether, these measurements show that $H_{3.6}IrO_4 \cdot 3.7H_2O$ undergoes three different redox processes in acidic conditions: the first one being a bulk diffusion-limited process at ~0.92 V vs RHE involving de-/intercalation of H_3O^+ within the structure of the layered iridate, a second non-diffusion-limited process at ~1.14 V vs RHE which can be attributed to the surface de-/protonation and a third oxidation process occurring at the OER potential.

2.4. Electronic signature of oxygen species in the hydrated iridate

Having established the unique ability for $H_{3.6}IrO_4 \cdot 3.7H_2O$ to reversibly exchange protons and structural water before and during the OER, our attention then turned to understanding the electronic properties of this phase. XAS measurements at the O K-edge were thus carried out. As shown in Figure 6a (and Figure S4), the peaks at ~ 527.8-528.5 eV for Sr_2IrO_4, ascribed to the transition to unoccupied O 2p hybridized with Ir 5d corresponding to t_{2g} and e_g frontier orbitals,[30] respectively, gained significant intensity with a shifting to lower energy after the H^+/Sr^{2+} cation exchange and the formation of $H_{3.6}IrO_4 \cdot 3.7H_2O$. A similar change of this pre-edge feature was previously observed for amorphous IrO_x at elevated potential during the OER,[31] and was explained by the formation of electrophilic "O^-" oxygen species following the deprotonation of the surface of the catalyst. This explanation would be consistent with the oxidation of Ir^{4+} in Sr_2IrO_4 into $Ir^{4.4+}$ in $H_{3.6}IrO_4.3.7H_2O$, as observed by XAS measurements at the Ir L-edge (Figure S6). This trend is also consistent with the O K-edge spectrum of α-$LiIr^{5+}O_3$, made from delithiation of Li_2IrO_3, which is known to undergo

lattice oxygen oxidation upon oxidation (grey line in Figure 6a). In order to assess this explanation, we intentionally removed structural water molecules from $H_{3.6}IrO_4 \cdot 3.7H_2O$ by vigorously shaking in water (Figures 6b and S6). This dehydration step was confirmed to be successful by coupling by TGA-MS (Figure 6c) which shows the sole loss of protons and no losses associated with structural water molecules (Figure 4d). Furthermore, ^1H NMR shows that protons bound to IrO_6 octahedra in H_4IrO_4 have a different average chemical shift of 11.9 ppm compared to $H_{3.6}IrO_4 \cdot 3.7H_2O$ (9.8 ppm, Figure 2) as a result of the lack of interactions with neighboring water molecules (Figure 6d). Lastly, a drastic loss of intensity is observed for the pre-edge feature of the dehydrated H_4IrO_4 (Figure 6a), which was located at an energy closer to Sr_2IrO_4 than $H_{3.6}IrO_4 \cdot 3.7H_2O$. These results suggest that the presence of structural water might be responsible for the presence of the low energy pre-edge feature previously ascribed to the formation of electrophilic "O^{-}" species. Therefore, caution must be exercised when attempting to identify surface species during the OER using the XAS data, especially for amorphous hydrated compounds such as IrO_x.

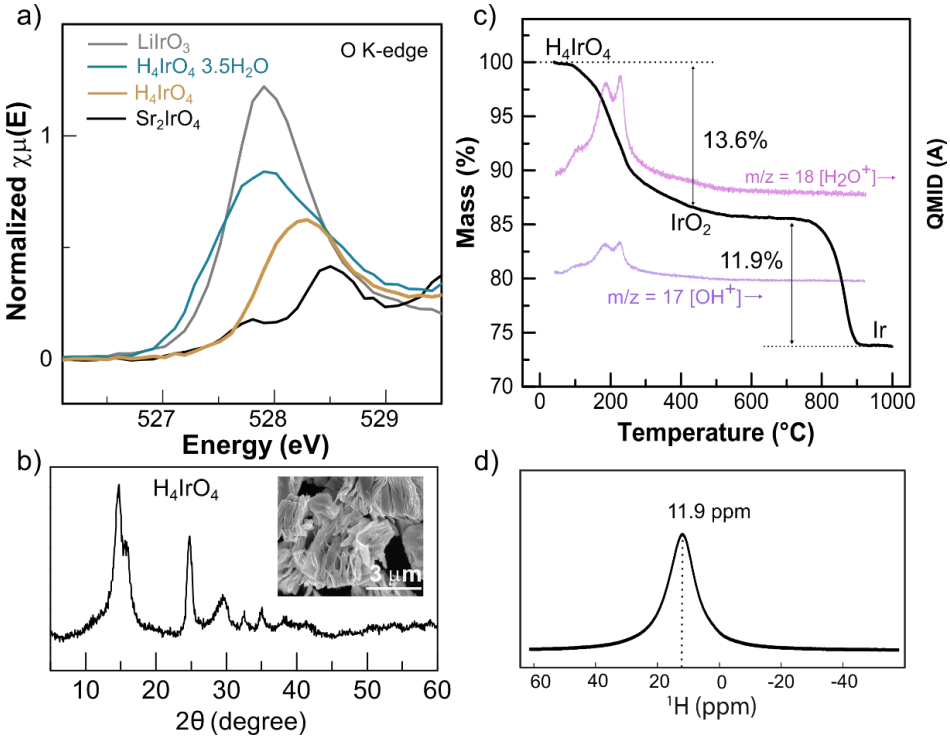

Figure 6. a Ex situ XAS measurements at the O K-edge recorded for $H_{3.6}IrO_4 \cdot 3.7H_2O$ compared to $LiIrO_3$, Sr_2IrO_4 as well as compared to the dehydrated H_4IrO_4 phase. **b** Powder XRD pattern, **c** TGA-MS data and **d** ^1H NMR spectra collected for the dehydrated H_4IrO_4 phase.

2.5. Toward the enhancement of the mass activity by exfoliation

While the specific activity of the newly obtained hydrated iridate $H_{3.6}IrO_4 \cdot 3.7H_2O$ was found among the best for Ir-based catalysts in acidic conditions (Figure 4b), the OER activity normalized by the mass of iridium is also of prime importance for the deployment of PEMWE at large scale, owing to the extreme scarcity of iridium.[4] In order to increase the mass normalized OER activity of $H_{3.6}IrO_4 \cdot 3.7H_2O$, we took advantage of its 2D structure to partially exfoliate the particles and thereby further increase the specific surface area. To do so, we employed a route previously reported for K_xIrO_y and $NaRuO_2$.[32][33] After Sr^{2+}/H^+ cationic exchange, the hydrated $H_{3.6}IrO_4 \cdot 3.7H_2O$ phase was stirred in a TBAOH solution for 7 days to insert TBA^+ inside the structure, followed by sonication for 1 h to induce full exfoliation (Figure 7a, see details in the Experimental section). The suspension containing the exfoliated iridate layers was directly drop-casted onto the glassy carbon electrodes for electrochemical measurements, while the concentration of iridium in the suspension was estimated by ICP-AES. By SEM imaging, we could confirm the relative success of the exfoliation where the micron-sized particles are found to break down into smaller ones (inserts in Figure 7a). Nevertheless, no homogeneous dispersion of single sheets was obtained, unlike previously reported for other layered compounds.[33] An enhancement of the OER current of a factor close to 2 at η = 300 mV can be seen comparing the mass normalized OER activity of these partially exfoliated particles with as-made $H_{3.6}IrO_4 \cdot 3.7H_2O$ (Figure 7b). This enhancement renders the mass normalized activity measured for this new hydrated phase second only to nano core-shell $IrNiO_x$ catalysts,[34] being competitive with IrO_x particles as small as 2nm. Therefore, with further optimization of the exfoliation procedure by either heating to improve the TBA^+ exchange into

the hydrated $H_{3.6}IrO_4 \cdot 3.7H_2O$ phase or by using a harsher sonication protocol, this newly obtained phase could even even overpass the mass activity for the best Ir-based nanocatalysts reported to date.

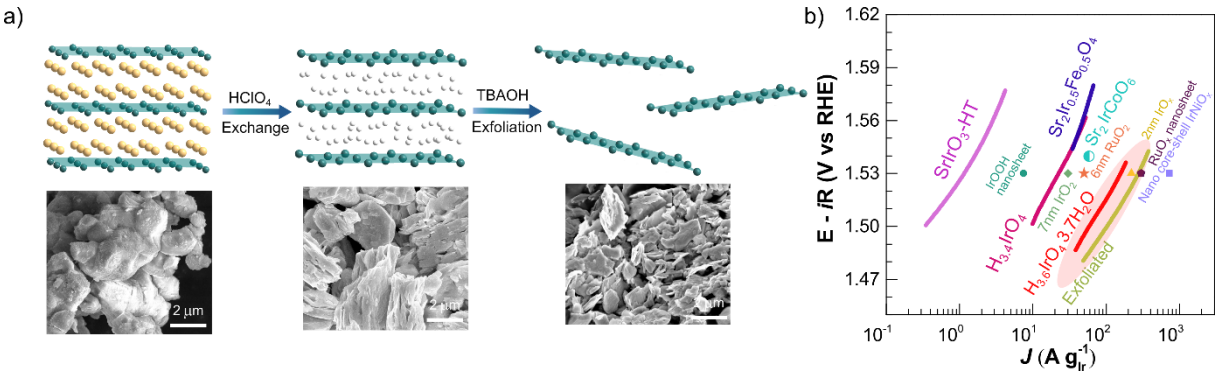

Figure 7. a Schematic representation of the cationic Sr^{2+}/H^+ exchange starting from Sr_2IrO_4 to form the hydrated $H_{3.6}IrO_4 \cdot 3.7H_2O$ phase followed by the exfoliation strategy to decrease the particle size of the newly obtained hydrated phase. **b** Tafel slope for the mass normalized OER activity of $H_{3.6}IrO_4 \cdot 3.7H_2O$ compared to results previously reported for selected iridium- and ruthenium-based catalysts (IrOOH nanosheet,[35] 7 nm IrO_2,[36] 6 nm RuO_2,[36] Sr_2IrCoO_6,[14] 2 nm IrO_x,[37] RuO_x nanosheet,[33] Nano core-shell $IrNiO_x$[34]).

2.6. Conclusion

In conclusion, we have demonstrated the first successful Sr^{2+}/H^+ cationic exchange in 2D Ruddlesden-Popper Sr_2IrO_4 to prepare a new protonated and hydrated compound, $H_{3.6}IrO_4 \cdot 3.7H_2O$. While this hydrated phase retains the corner-shared IrO_6 octahedra framework from the parent Ruddlesden-Popper phase, gliding of the sheets of IrO_6 octahedra was observed, resulting in their alignment along the c-axis. Though this unique structural configuration is extremely unfavored for a RP phase, the protonation of the apical oxygen screens the charge from the oxygen anions and hence stabilizes the structure. In addition, the intercalation of interstitial water molecules further stabilizes the structure through hydrogen bonds forming

between the protonated apical oxygen and the water molecules. The newly obtained hydrated iridate phase shows very promising performance as OER catalyst in acidic conditions, with a BET-normalized activity outperforming IrO_2 and some perovskites (e.g. 6H-$SrIrO_3$), while approaching to those reported for $SrIrO_3$ epitaxial films. More importantly, our stability study shows that while 6H-$SrIrO_3$ is unstable in acidic conditions under anodic polarization, the newly obtained $H_{3.6}IrO_4 \cdot 3.7H_2O$ phase shows relatively limited iridium leaching as well as stable performance under these drastic conditions. Coupling the electrochemical study with ex situ XRD data, we could postulate that this improved stability is in part due to the reversible exchange of protons as well as structural water occurring prior and during the OER. Indeed, these exchanges, especially the proton exchange, allows for the phase to counterbalance the charge associated with the OER and therefore help to avoid the formation of soluble Ir^{3+} or IrO_4^{2-} species which has been considered as the dominating iridium dissolution mechanism.[17][19] Finally, we demonstrate the flexibility of this new 2D phase which can be partially exfoliated to decrease the particle size and reach mass normalized OER performances competing with the ones previously reported for 2nm IrO_x particles. We therefore believe that such hydrated 2D structure represents a unique opportunity to 1) limit the drastic iridium leaching often encountered for complex iridium-based catalysts, and 2) achieve greater mass normalized OER performances, which is a prerequisite for scaling up clean production of H_2 by using PEMWE.

3. Experimental Section

Synthesis: Sr_2IrO_4 and 6H-$SrIrO_3$ were prepared using a conventional ceramic method as described in previous paper.[38][39] In brief, suitable amount of $SrCO_3$ and Ir black were finely ground and pre-sintered at 900 °C before pressing into a 13 mm diameter pellet. The pellet was then heated in air for 24 h at 1250 °C for Sr_2IrO_4 and 1200°C for 6H-$SrIrO_3$ to obtain a single

phase. For the preparation of $H_{3.6}IrO_4 \cdot 3.7H_2O$, Sr_2IrO_4 powder was stirred in 0.1 M $HClO_4$ for 12 h, then recovered by centrifugation and dried at 55 °C under vacuum for 4 h.

Materials Characterization: X-ray diffraction (XRD) data were collected using a BRUKER D8 Advance diffractometer with Cu Ka radiation ($\lambda_{k\alpha1}$ = 1.54056 Å, $\lambda_{k\alpha2}$ = 1.54439 Å).

TGA-MS were carried out by heating around 10 to 15 mg of samples under high purity Ar gas from room temperature to 1000 °C at a rate of 5 K min^{-1}.

Solid state ^1H NMR were recorded on a Bruker 4.7 T Avance III spectrometer mounted with a 1.3 mm double-resonance probe head tuned to ^1H at 200 MHz. A 1.3 mm rotor, packed with the sample, was spinning at a 64 kHz MAS rate under nitrogen at room temperature, with no temperature regulation, assuming that the internal rotor temperature is around 60−70 °C due to friction effects. The chemical shifts were referenced at 0 ppm with respect to TMS for ^1H and the RF field strength was set to 287 kHz for ^1H. All 1D spectra were obtained with a rotor synchronized Hahn echo sequence, with a total echo time of two rotor periods (31.25 μs). The 2D EXSY and RFDR sequence have been described in previous works.[40]

TEM samples were prepared in air by crushing the crystals in a mortar in ethanol and depositing drops of suspension onto holey carbon grids. Electron diffraction (ED) patterns and high angle annular dark field scanning transmission electron microscopy (HAADF-STEM) images were obtained with an aberration-corrected Titan G3 electron microscope operated at 200 kV.

X-ray absorption spectroscopy (XAS) measurements at the Ir L_3-edge were carried out at the B18 XAS beamline at the Diamond Light Source. The normalization was done using the Athena software.

Ex situ XAS measurement at the O K-edge were collected on Beamline 4-ID-C of the Advanced Photon Source (APS) at Argonne National Laboratory. Normalization of the spectra as well as the fitting procedure were done using the Athena software. The absorption step was reproduced using an error function. Gaussian curves were used to fit the peak positions of the normalized XAS spectra.

Brunauer–Emmett–Teller (BET) specific surface areas were measured by N_2 porometry at 77 K using a Micromeritics Triflex instrument. Before measurements, samples were de-gassed on a Micromeritics Smart VacPrep device for 5 h at 55° C for protonated iridates and 150°C for other oxides. The specific surface area was calculated using BET equations.

For ICP-OES, ~2 mg of active materials were loaded onto a 2*2 cm^2 glassy carbon electrode. The electrode was then held at a current density of 1 mA/cm_{oxide}^2 for 1 h in 20 mL of 0.1 M $HClO_4$ electrolytes. 5 mL of electrolyte was taken for the measurements. For the protonated iridate $H_{3.6}IrO_4 \cdot 3.7H_2O$, 2 mg of Sr_2IrO_4 was used and soaked in 20 mL of electrolyte for 10 min to allow for sufficient cation exchange prior to the galvanostatic step. Sr and Ir elements were measured for each sample on a ThermoFisher iCAP 6000 device. Line 346.4, 407.7, 421.5 were used for Sr, and 212.6, 224.2,236.8 for Ir. The detection error bar of the instrument is ~ 5 to 10%.

Electrochemical Characterization: Electrochemical measurements were carried out at room temperature using a VMP-300 potentiostat (Biologic Co., Claix, France) with a conventional three-electrodes configuration: a glassy carbon electrode with geometric surface area of 0.196 cm^2 as the working electrode, a saturated Ag/AgCl electrode with a potential of 200 mV vs. SHE as the reference electrode, and a Pt wire as the counter electrode. The reference electrode was calibrated versus a reversible hydrogen electrode (Gaskatel) prior to the measurements. The CV measurements were performed in 0.1 M $HClO_4$ electrolyte at a scan rate of 10 mVs^{-1} (except for Figure 5a and 5b) with a rotating speed of 1600 rpm. Potentials are corrected with iR drop and reported versus RHE (Resistance ≈ 28 to 32 Ω for 0.1 M $HClO_4$). The catalysts were drop-casted onto the working electrode. The drop-casting ink was prepared by dispersing 10 mg catalyst powders and 1 mg ethylene black carbon (Alfa Aesar 99.9%) in 1.940 mL of tetrahydrofuran (THF; Sigma-Aldrich 99.9%) and 0.060 mL of Nafion binder (5% weight, Ion Power). The loading of active material was 50 μg (10 μL ink) per electrode.

Ex situ XRD: Ex situ XRD data as shown in Figure 5d were collected at different potentials on self-standing PTFE electrodes. The PTFE electrodes were prepared by mixing $H_{3.6}IrO_4 \cdot 3.7H_2O$ together with 10 wt% ethylene black carbon and 5 wt% PTFE in ethanol, and then laminating the paste several times to obtain films of ~ 25 μm thickness. The three electrodes used were glassy carbon rods with a piece of the PTFE film as the working electrode, calomel electrode (0.240 V vs. SHE) as the reference electrode and YP50 Carbon as the counter electrode. The working and counter electrodes were separated using 3 Whatman glass fiber separators fully soaked in the 0.1 M $HClO_4$ electrolyte.

Exfoliation: $H_{3.6}IrO_4 \cdot 3.7H_2O$ powders were stirred in a TBAOH solution for 7 days until a suspension with an indigo-blue color was obtained. The suspension was then sonicated for 1 h for further exfoliation. As TBA^+ ions form insoluble salts in $HClO_4$ electrolytes, the suspension was centrifuged at 6000 rpm for 1 h and washed twice with H_2O to remove the excess TBA^+ ions. The concentration of iridium in the final suspension was detected by ICP-MS and this suspension was drop-casted on glassy carbon electrodes for electrochemical measurements.

Supporting Information

Supporting Information is available from the Wiley Online Library or from the author.

Acknowledgements

A.G. and R.Z. acknowledge financial support from the ANR MIDWAY (Project ID ANR-17-CE05-0008). J.C. and H.L. were supported by the National Science Foundation under grant no. DMR-1809372. We acknowledge Diamond Light Source for time awarded to the Energy Materials BAG on Beamline B18, under Proposal sp12559. Use of the Advanced Photon Source at Argonne National Laboratory was supported by the US Department of Energy under contract no. DE-AC02-06CH11357.

Received: ((will be filled in by the editorial staff))
Revised: ((will be filled in by the editorial staff))
Published online: ((will be filled in by the editorial staff))

References

[1] E. Willinger, C. Massué, R. Schlögl, M. G. Willinger, *J. Am. Chem. Soc.* **2017**, *139*,

12093.

[2] M. Carmo, D. L. Fritz, J. Mergel, D. Stolten, *Int. J. Hydrogen Energy* **2013**, *38*, 4901.

[3] P. C. K. Vesborg, T. F. Jaramillo, *RSC Adv.* **2012**, *2*, 7933.

[4] J. Kibsgaard, I. Chorkendorff, *Nat. Energy* **2019**, *4*, 430.

[5] C. Wei, R. R. Rao, J. Peng, B. Huang, I. E. L. Stephens, M. Risch, Z. J. Xu, Y. Shao-Horn, *Adv. Mater.* **2019**, *31*, 1806296.

[6] M. Bernt, A. Siebel, H. A. Gasteiger, *J. Electrochem. Soc.* **2018**, *165*, F305.

[7] Y. Zhao, E. A. Hernandez-Pagan, N. M. Vargas-Barbosa, J. L. Dysart, T. E. Mallouk, *J. Phys. Chem. Lett.* **2011**, *2*, 402.

[8] M. Yagi, E. Tomita, T. Kuwabara, *J. Electroanal. Chem.* **2005**, *579*, 83.

[9] J. Gao, C. Xu, S. Hung, W. Liu, W. Cai, Z. Zeng, C. Jia, H. M. Chen, H. Xiao, J. Li, Y. Huang, B. Liu, *J. Am. Chem. Soc.* **2019**, *141*, 3014.

[10] A. Grimaud, O. Diaz-Morales, B. Han, W. T. Hong, Y. L. Lee, L. Giordano, K. A. Stoerzinger, M. T. M. Koper, Y. Shao-Horn, *Nat. Chem.* **2017**, *9*, 457.

[11] L. C. Seitz, C. F. Dickens, K. Nishio, Y. Hikita, J. Montoya, A. Doyle, C. Kirk, A. Vojvodic, H. Y. Hwang, J. K. Norskov, T. F. Jaramillo, *Science (80-.).* **2016**, *353*, 1011 LP.

[12] Y. Chen, H. Li, J. Wang, Y. Du, S. Xi, Y. Sun, M. Sherburne, J. W. Ager, A. C. Fisher, Z. J. Xu, *Nat. Commun.* **2019**, *10*, 572.

[13] O. Diaz-Morales, S. Raaijman, R. Kortlever, P. J. Kooyman, T. Wezendonk, J. Gascon, W. T. Fu, M. T. M. Koper, *Nat. Commun.* **2016**, *7*, 12363.

[14] R. Zhang, N. Dubouis, M. Ben Osman, W. Yin, M. T. Sougrati, D. A. D. Corte, D. Giaume, A. Grimaud, *Angew. Chemie - Int. Ed.* **2019**, *58*, 4571.

[15] S. Cherevko, S. Geiger, O. Kasian, N. Kulyk, J. P. Grote, A. Savan, B. R. Shrestha, S. Merzlikin, B. Breitbach, A. Ludwig, K. J. J. Mayrhofer, *Catal. Today* **2016**, *262*, 170.

[16] Y.-T. Kim, P. P. Lopes, S.-A. Park, A.-Y. Lee, J. Lim, H. Lee, S. Back, Y. Jung, N.

Danilovic, V. Stamenkovic, J. Erlebacher, J. Snyder, N. M. Markovic, *Nat. Commun.* **2017**, *8*, 1449.

[17] P. Pearce, C. Yang, A. Iadecola, J. Rodriguez-Carvajal, G. Rousse, R. Dedryvère, A. M. Abakumov, D. Giaume, M. Deschamps, J.-M. Tarascon, A. Grimaud, *Chem. Mater.* **2019**, *31*, 5845.

[18] R. Zhang, P. E. Pearce, Y. Duan, N. Dubouis, T. Marchandier, A. Grimaud, *Chem. Mater.* **2019**, *31*, 8248.

[19] O. Kasian, J.-P. Grote, S. Geiger, S. Cherevko, K. J. J. Mayrhofer, *Angew. Chemie Int. Ed.* **2018**, *57*, 2488.

[20] A. J. Perez, R. Beer, Z. Lin, E. Salager, P. Taberna, A. M. Abakumov, P. Simon, J. Tarascon, *Adv. Energy Mater.* **2018**, *8*, 1702855.

[21] Y. Chen, H. Li, J. Wang, Y. Du, S. Xi, Y. Sun, M. Sherburne, J. W. Ager, A. C. Fisher, Z. J. Xu, *Nat. Commun.* **2019**, *10*, 572.

[22] S. Geiger, O. Kasian, M. Ledendecker, E. Pizzutilo, A. M. Mingers, W. T. Fu, O. Diaz-Morales, Z. Li, T. Oellers, L. Fruchter, A. Ludwig, K. J. J. Mayrhofer, M. T. M. Koper, S. Cherevko, *Nat. Catal.* **2018**, *1*, 508.

[23] J. D. Jorgensen, B. Dabrowski, S. Pei, D. R. Richards, D. G. Hinks, *Phys. Rev. B* **1989**, *40*, 2187.

[24] F. Girgsdies, R. Schöllhorn, *Solid State Commun.* **1994**, *91*, 111.

[25] D. Weber, L. M. Schoop, D. Wurmbrand, J. Nuss, E. M. Seibel, F. F. Tafti, H. Ji, R. J. Cava, R. E. Dinnebier, B. V Lotsch, *Chem. Mater.* **2017**, *29*, 8338.

[26] K. Lee, M. Osada, H. Y. Hwang, Y. Hikita, *J. Phys. Chem. Lett.* **2019**, *10*, 1516.

[27] R. Tang, Y. Nie, J. K. Kawasaki, D.-Y. Kuo, G. Petretto, G. Hautier, G.-M. Rignanese, K. M. Shen, D. G. Schlom, J. Suntivich, *J. Mater. Chem. A* **2016**, *4*, 6831.

[28] K. Xu, F. Song, J. Gu, X. Xu, Z. Liu, X. Hu, *J. Mater. Chem. A* **2018**, *6*, 14240.

[29] J. D. Blakemore, N. D. Schley, M. N. Kushner-Lenhoff, A. M. Winter, F. D'Souza, R.

H. Crabtree, G. W. Brudvig, *Inorg. Chem.* **2012**, *51*, 7749.

[30] A. Grimaud, K. J. May, C. E. Carlton, Y.-L. Lee, M. Risch, W. T. Hong, J. Zhou, Y. Shao-Horn, *Nat. Commun.* **2013**, *4*, 2439.

[31] V. Pfeifer, T. E. Jones, J. J. Velasco Vélez, C. Massué, M. T. Greiner, R. Arrigo, D. Teschner, F. Girgsdies, M. Scherzer, J. Allan, M. Hashagen, G. Weinberg, S. Piccinin, M. Hävecker, A. Knop-Gericke, R. Schlögl, *Phys. Chem. Chem. Phys.* **2016**, *18*, 2292.

[32] D. Takimoto, K. Fukuda, S. Miyasaka, T. Ishida, Y. Ayato, D. Mochizuki, W. Shimizu, W. Sugimoto, *Electrocatalysis* **2017**, *8*, 144.

[33] S. Laha, Y. Lee, F. Podjaski, D. Weber, V. Duppel, L. M. Schoop, F. Pielnhofer, C. Scheurer, K. Müller, U. Starke, K. Reuter, B. V Lotsch, *Adv. Energy Mater.* **2019**, *9*, 1803795.

[34] H. N. Nong, T. Reier, H.-S. Oh, M. Gliech, P. Paciok, T. H. T. Vu, D. Teschner, M. Heggen, V. Petkov, R. Schlögl, T. Jones, P. Strasser, *Nat. Catal.* **2018**, *1*, 841.

[35] D. Weber, L. M. Schoop, D. Wurmbrand, S. Laha, F. Podjaski, V. Duppel, K. Müller, U. Starke, B. V Lotsch, *J. Mater. Chem. A* **2018**, *6*, 21558.

[36] Y. Lee, J. Suntivich, K. J. May, E. E. Perry, Y. Shao-Horn, *J. Phys. Chem. Lett.* **2012**, *3*, 399.

[37] P. Lettenmeier, J. Majchel, L. Wang, V. A. Saveleva, S. Zafeiratos, E. R. Savinova, J.-J. Gallet, F. Bournel, A. S. Gago, K. A. Friedrich, *Chem. Sci.* **2018**, *9*, 3570.

[38] A. J. Gatimu, R. Berthelot, S. Muir, A. W. Sleight, M. A. Subramanian, *J. Solid State Chem.* **2012**, *190*, 257.

[39] I. Qasim, B. J. Kennedy, M. Avdeev, *J. Mater. Chem. A* **2013**, *1*, 3127.

[40] R. J. Messinger, M. Ménétrier, E. Salager, A. Boulineau, M. Duttine, D. Carlier, J.-M. Ateba Mba, L. Croguennec, C. Masquelier, D. Massiot, M. Deschamps, *Chem. Mater.* **2015**, *27*, 5212.

The table of contents entry should be 50–60 words long and should be written in the present tense and impersonal style (i.e., avoid we). The text should be different from the abstract text.

Keyword Electrocatalysis

*Ronghuang Zhang, Paul E. Pearce, Vanessa Pimenta, Mathieu Courty, Jordy Cabana, Heifang Li, Daniel Alves Dalla Corte, Artem M. Abakumov, Gwenaelle Rousse, Domitille Giaume, Michael Deschamps, Alexis Grimaud**

First example of protonation of Ruddlesden-Popper Sr_2IrO_4: a route to better water oxidation catalysts

ToC figure ((Please choose one size: 55 mm broad × 50 mm high **or** 110 mm broad × 20 mm high. Please do not use any other dimensions))

((Supporting Information can be included here using this template))

Supporting Information

First example of protonation of Ruddlesden-Popper Sr_2IrO_4: a route to better water oxidation catalysts

*Ronghuang Zhang, Paul E. Pearce, Vanessa Pimenta, Mathieu Courty, Jordy Cabana, Heifang Li, Daniel Alves Dalla Corte, Artem M. Abakumov, Gwenaelle Rousse, Domitille Giaume, Michael Deschamps, Alexis Grimaud**

E-mail: alexis.grimaud@college-de-france.fr

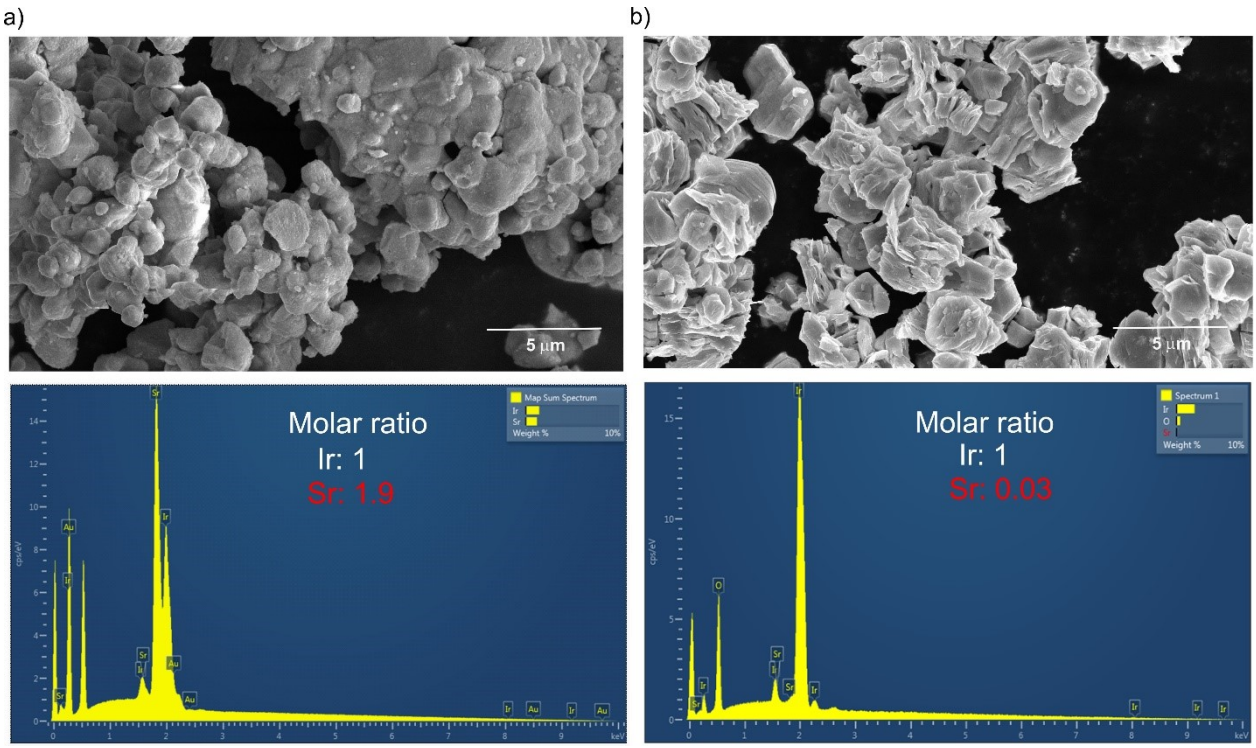

Figure S1. Scanning electron microscopy (SEM) and energy-dispersive X-ray (EDX) analysis of a) parent Sr_2IrO_4 and b) $H_{3.6}IrO_4 \cdot 3.7H_2O$ where the concentration of strontium is negligible according to the detection limit of the instrument, suggesting a complete dissolution of Sr^{2+} from Sr_2IrO_4 to form the protonated iridate.

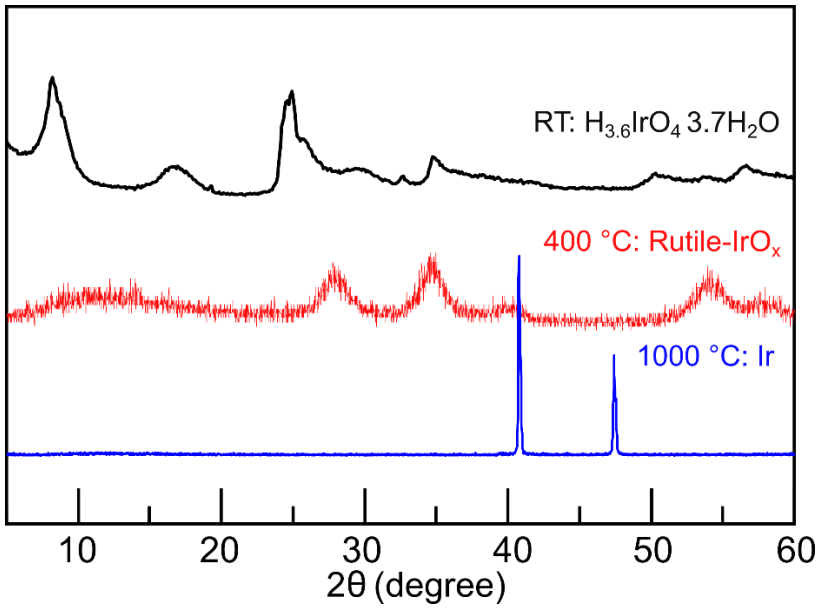

Figure S2. XRD diagram collected for the $H_{3.6}IrO_4 \cdot 3.7H_2O$ phase after heat treatments at different temperatures.

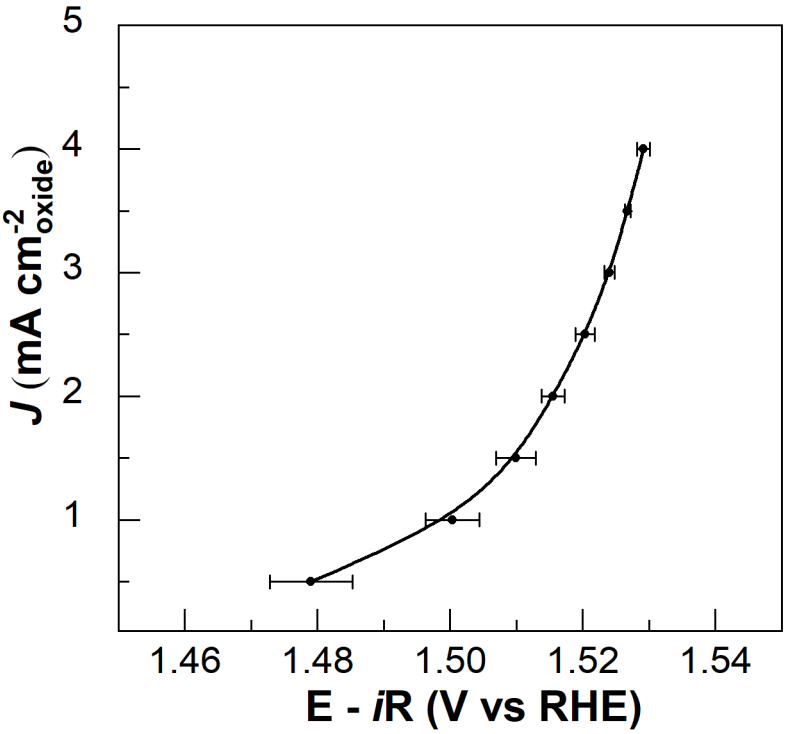

Figure S3. Representative CV scans with error bar obtained from the cation-exchanged phase $H_{3.6}IrO_4 \cdot 3.7H_2O$.

Table S1. Electrochemical conditions (applied currents and measured potentials) for the galvanostatic test at 1.0 mA/cm$^2_{oxide}$ for 1 h used for the iridium dissolution study by ICP-OES.

	Applied current/mA	Potential (V vs. RHE)
$H_{3.6}IrO_4 \cdot 3.7H_2O$	60	1.60
$H_{3.5}IrO_4$	44	1.65
6H-$SrIrO_3$	20	1.61
$Sr_2Ir_{0.5}Fe_{0.5}O_4$	14	1.51

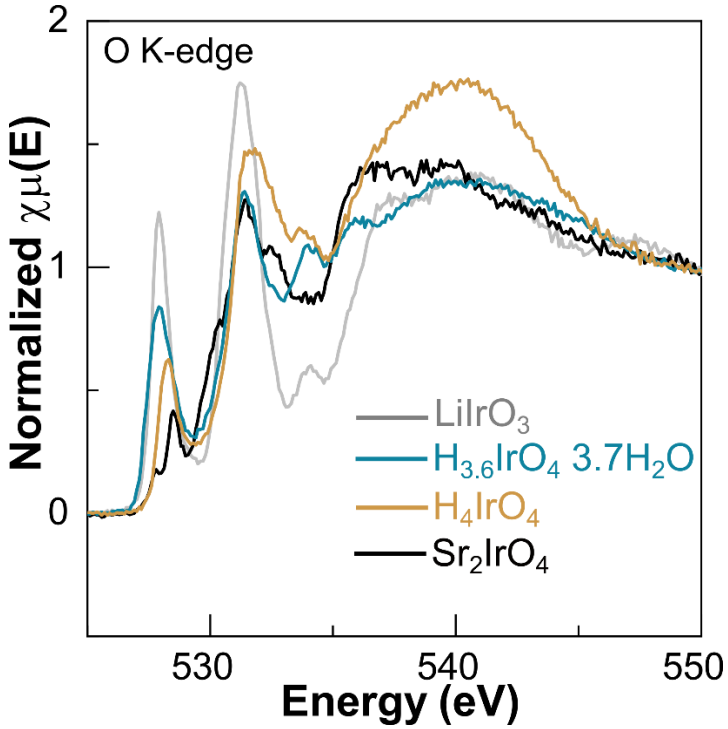

Figure S4. XAS measurements at the O K-edge in total fluorescent yield (TFY) mode recorded for $H_{3.6}IrO_4 \cdot 3.7H_2O$ and compared to $LiIrO_3$, Sr_2IrO_4 as well as to the dehydrated H_4IrO_4 phase.

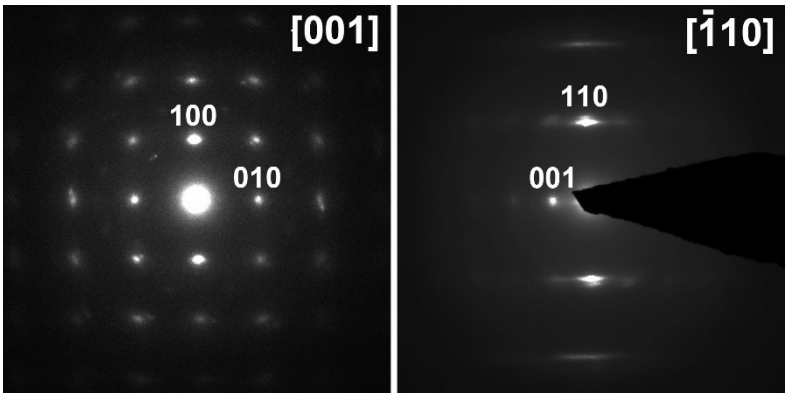

Figure S5. Electron diffraction (ED) data for H_4IrO_4, which can be indexed into a similar unit cell as that of $H_{3.6}IrO_4 \cdot 3.7H_2O$ with an orthorhombically distortion, suggesting that the structural framework of $H_{3.6}IrO_4 \cdot 3.7H_2O$ was retained during the removal of structural water.

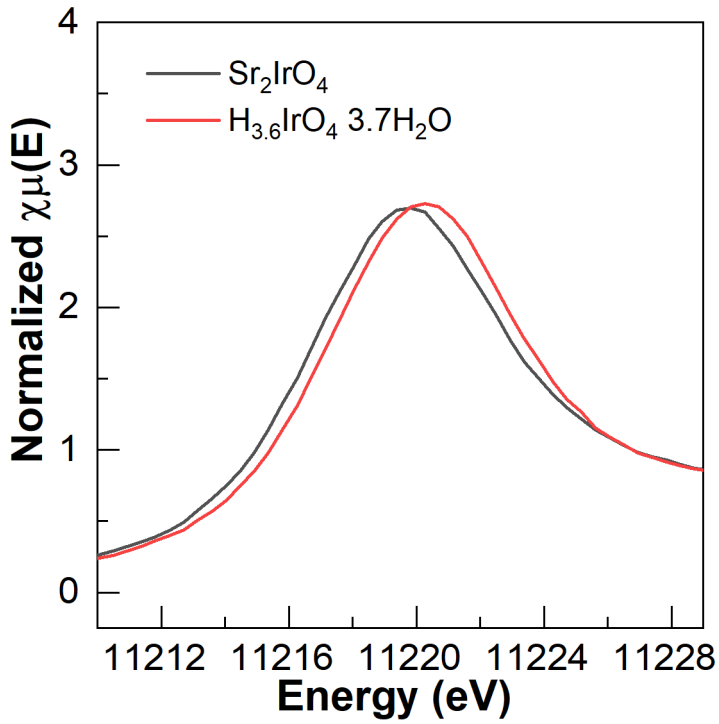

Figure S6. XAS measurements at the Ir L_3-edge (TEY) recorded for $H_{3.6}IrO_4 \cdot 3.7H_2O$ compared to that of Sr_2IrO_4.